Assessment of interface passivation in AgBiS$_2$ Q-dot sensitized solar cell on the carrier transport and recombination

Dimuthumal Rajakaruna [a], Hong-yi Tan [b], Chang-Feng Yan [b], Jayasundera Bandara [a],*

[a] National Institute of Fundamental Studies, Hantana Road, CP 20000, Kandy, Sri Lanka
[b] Guangzhou Institute of Energy Conversion, Chinese Academic of Sciences, No.2 Nengyuan Road, Wushan, Tianhe District, Guangzhou, 510640, China

ARTICLE INFO

ABSTRACT

Silver bismuth sulfide has been discovered to be an appropriate light-harvesting material but the carrier transport restrictions and trap-assisted recombination in Q-dot AgBiS$_2$ limit the device efficiency. To address inherent charge carrier transport restrictions and trap-assisted recombination in q-dot AgBiS$_2$, this work studied the effect of interface passivation of AgBiS$_2$ Q-dot by a thin-nanostructured ZnS layer on carrier transport and recombination. The charge-transfer and carrier recombination processes investigated by open-circuit voltage decay curves and electrochemical impedance spectroscopy indicate the decrease in inherent trap-assisted Shockley-Read-Hall (SRH) recombination in bare AgBiS$_2$ due to the passivation of AgBiS$_2$ by ZnS while an increase in the charge recombination resistance and improvement in carrier lifetime resulting in enhanced solar cell performance. A very thin ZnS passivation layer on AgBiS$_2$ also boosts the light absorption, resulting in a red shift in the light absorption peak. The formation of AgBiS$_2$ and ZnS was confirmed by XRD, EDS, and TEM analysis and the explicit role of the ZnS passivation layer on the electron transport layer and the light harvesting AgBiS$_2$ Q-dots was investigated. Using a polysulfide electrolyte and optimal ZnS layers on TiO$_2$ and AgBiS$_2$ nanostructures in the FTO/m-TiO$_2$/ZnS(1)/AgBiS$_2$/ZnS(2) electrode design enhanced the efficiency and the passivation can also be implemented for a solid-hole transport material.

1. Introduction

Ternary semiconductor materials with an ideal bandgap, environmental friendliness, and a broad absorption range are considered next-generation photovoltaic materials. Especially, silver bismuth sulfide (AgBiS$_2$) which is a non-toxic, earth-abundant light-harvesting material with a high absorption coefficient, high mobility, and easily tunable band gap has been reported in diverse applications [1–4] As a result of current surge in interest in AgBiS$_2$-based thin film solar cells, a remarkable efficiency of 10 % for sub-micron-grain AgBiS$_2$ thin films synthesized via vapor-assisted solution process treatment has been achieved [5] Though the progress of AgBiS$_2$ q-dot sensitized solar cells is not dramatic as thin-film AgBiS$_2$ solar cells, a notable progress has been accomplished, reporting 2.87 and 0.5 % efficiencies for solid hole-conductors and for the polysulfide liquid-electrolyte respectively [2,6–9] Although the efficiency of AgBiS$_2$ sensitized solar cells is lower than that of DSSC, the use of AgBiS$_2$ quantum dots as the light-absorber allows for harvesting the full solar spectrum by fine control of the band gap, resulting in higher solar cell performance compared to DSSC.

Theoretical investigation of electronic, optical, photovoltaic and thermoelectric properties of AgBiS$_2$ with a band gap energy of 1.07 eV, and an absorption coefficient of $\sim10^6$ cm^{-1} revealed that it can achieve a short-circuit current density (Jsc) of 22 mA/cm^2 and a conversion efficiency of 20 % [10] The experimentally reported Jsc and efficiency for AgBiS$_2$ Q-dots solar cells are significantly lower than the theoretically expected Jsc and efficiency and mainly attributed to the high-density trap states and energy disorder in AgBiS$_2$ resulting in energy loss during charge carrier transport and collection [11,12] To overcome energy loss in AgBiS$_2$ based solar cells, several strategies such as use of larger grain AgBiS$_2$ [13], cation disorder engineering [14], solvent-engineering-assisted ligand exchange strategy [15], mixed AgBiS$_2$ nanocrystals [16,17], halide ions passivation of AgBiS$_2$ surface [17] and nanowire heterojunction solar cells [18,19] have been reported. i.e. Senina et al., was able to achieve a power conversion efficiency of 6.4 %, by obtaining larger size colloidal AgBiS$_2$ nanocrystals, that resulted in lower grain boundaries and enhanced mobility and reduced trap-assisted recombination [6] On the other hand, Wang et al. reported efficient solar cells via cation disorder engineering of AgBiS2

---

* Corresponding author.
  E-mail address: jayasundera.ba@nifs.ac.lk (J. Bandara).

nanocrystals [14] To improve the surface chemistry and fabrication of the AgBiS$_2$Q-dots solar cell, Zhong et al., implemented a solvent engineering-based ligand exchange method and achieved a PCE of up to 8.95 % [15] By employing AgBiS$_2$ nanocrystals of different sizes Burgués-Ceballos et al. [20] and Oh et al. [16] aligned different Q-dot AgBiS$_2$ nanocrystals to introduce a potential gradient enabling enhanced carrier transport resulting in enhanced power conversion efficiency. By coordinating different halide ligands with AgBiS$_2$ nanocrystals, Xiao et al., reported the enhanced charge carrier transport properties of AgBiS$_2$ and hence improved solar cell performance due to superior passivation which depended on the ligand type and the coverage [17] Adding metal ions, such as sodium (Na), improved solar cell efficiency by producing a covering layer on AgBiS$_2$ that passivates trap states and reduces charge recombination [21] It has been reported that the hydrothermal synthesis and molecular precursor-based approach can be employed to control of the morphology and surface states of AgBiS$_2$ nanocrystals, both of which are critical for enhancing the efficiency of the solar cells [22,23]

To improve the performance of quantum-dot-sensitized solar cells, the charge transfer across interfaces in quantum-dot solar cells should be investigated, especially given the large specific interface area of nanomaterials in these cells. Therefore, efforts have focused on modifying the interface structure with passivation layers. One often used approach in alleviating the intrinsic surface imperfections in ternary semiconductor materials is the surface and interface passivation [24–26] As a result, more passivation strategies such as organic ligand and inorganic passivating materials are being developed in recently. Passivating AgBiS$_2$ Q-dots with organic ligands was shown to reduce interface recombination and minimize current leakage, resulting in dramatically better photovoltaic performance [27] Adding a 2-mercaptoethanol ligand to the TMAI has been shown to improve the passivation of AgBiS$_2$ by lowering the trap density and altering the energy levels for more favorable carrier transfer to the HTL [28] Despite successful passivation of AgBiS$_2$ by organic ligands, the key constraints to increasing device efficiency are low open-circuit voltage (Voc) and Jsc. Although it is well known that inorganic materials can be used to passivate Q-dot solar cells [29], the passivation of AgBiS$_2$ nanocrystals by inorganic passivation materials has received little attention [24] It is expected that selecting a similar lattice structure to AgBiS$_2$ nanocrystals will increase passivation effect and hence, in this study, we investigated the impact of interface passivation by a ZnS layer on the efficiency of AgBiS$_2$ Q-dot-sensitized solar cells and address the carrier losses (i.e. trapping of charges at the surface defects at the TiO$_2$/AgBiS$_2$ interface, recombination at the AgBiS$_2$/electrolyte interface, inherent internal trap states in AgBiS$_2$, recombination of electrons in TiO$_2$ with trapped holes in AgBiS$_2$ Q-dots and oxidized polysulfide species, as do electrons in FTO). The passivation effect on AgBiS$_2$ Q-dot-based solar cells was examined using a liquid electrolyte since it allows for easy manipulation of interface parameters, but it can also be applied to solid electrolytes or hole-conducting materials.

2. Experimental section

2.1. Preparation of electron transport layer (ETL)

The TiO$_2$ mesoporous layer was fabricated by applying a TiO$_2$ paste onto the FTO glass using a modified Pichini method [24] The TiO$_2$ paste was synthesized as follows: first, 1.33 ml of ethylene glycol was heated to 60 °C, after which 0.31 ml of titanium isopropoxide and 1.27 g of citric acid were added. The mixture was heated further to 90 °C for 15 min. Once the solution cleared, it was cooled to room temperature and mixed with 0.56 g of P25 Degussa TiO$_2$ powder, then ground for one hour. The ratios of titanium isopropoxide to citric acid to ethylene glycol were maintained at 1:6:24, while the ratio of titanium isopropoxide to TiO$_2$ was 1:7. The prepared paste was applied to a cleaned fluorine-doped tin oxide (FTO, 7 Ω cm^{-2}, Solaronix) film using the doctor

blade method. The TiO$_2$ mesoporous layer was ensured to be of uniform thickness by using one layer of Scotch tape. This coated film was then sintered at 450 °C with a gradual temperature increase of 3 °C per minute.

2.2. Preparation of silver bismuth sulfide quantum dot

AgBiS$_2$ quantum dots were synthesized using the Successive Ionic Layer Adsorption and Reaction (SILAR) method [1,30,31] Each SILAR cycle involved the following steps: first, immersing the TiO$_2$ film in a 0.017 M AgNO$_3$ aqueous solution for 30 s, followed by rinsing in deionized water for another 30 s. Next, the Ag$^+$-impregnated electrode was immersed in a 0.025 M Na$_2$S aqueous solution for 30 s and then rinsed in deionized water for another 30 s. The electrode was then immersed in a 0.025 M Bi(NO$_3$)$_3$ solution (Bi(NO$_3$)$_3$ dissolved in a mixture of distilled water and acetic acid) for 30 s, followed by rinsing in deionized water for 30 s. Afterward, the Ag$^+$/S^{2-}/Bi^{3+}-impregnated electrode was immersed in a 0.025 M Na$_2$S aqueous solution for 30 s and rinsed again in deionized water for 30 s. To ensure high-quality films, it was essential to air-dry the electrodes at room temperature after each immersion step. After deposition, the AgBiS$_2$ Q-dots, electrodes were kept overnight and subsequently annealed at 100 °C for one hour on a hotplate in ambient air.

2.3. Preparation of ZnS thin passivation layer

In the first case, a ZnS layer was deposited between the TiO$_2$/**ZnS (1)**/AgBiS$_2$ interface using the SILAR method. A TiO$_2$ film on the FTO substrate was immersed in a 0.05 M Zn(Ac)$_2$ solution for 1 min and then rinsed with deionized water. The Zn^{2+}-impregnated FTO/TiO$_2$ electrode was subsequently dipped in a 0.05 M Na$_2$S solution for 1 min and rinsed again, completing one SILAR cycle to form FTO/TiO$_2$/**ZnS(1)**. In the second case, a ZnS passivation layer was deposited on the AgBiS$_2$ layer (TiO$_2$/AgBiS$_2$/**ZnS(2)**/polysulfide) using the same SILAR method. In the third case, a ZnS passivation layer was deposited at both the TiO$_2$/**ZnS (1)**/AgBiS$_2$/**ZnS(2)**/polysulfide interfaces using the same SILAR method.

2.4. Preparation of Polysulfide electrolyte and Cu$_2$S coated brass counter electrode

The polysulfide electrolyte was prepared by dissolving 2 M Na$_2$S, 2 M S, and 0.2 M KCl in a mixture of methanol and water in a 7:3 (v/v) ratio. To prepare a Cu$_2$S/brass counter electrode (CE), a brass plate was immersed in concentrated HCl at 90 °C and heated until all the HCl evaporated. Subsequently, the brass plate was thoroughly washed with distilled water and dried. A Parafilm spacer with a hole was placed on top of the cleaned brass plate (treated with boiled HCl), after which the prepared polysulfide electrolyte was applied to the exposed area of the brass plate [24]

2.5. Device Fabrication

The solar cell assembled by sandwiching FTO/TiO$_2$/**ZnS(1)**/AgBiS$_2$/ **ZnS(2)** working electrode and the Cu$_2$S/Brass counter electrode using a binder clip and by introducing the polysulfide electrolyte in between the working electrode and the Cu$_2$S/Brass counter electrode. The active area of the testing device is 0.25 cm^2.

2.6. Characterization

Thermal Field Emission (Analytical) Scanning Electron Microscope (S4800, Hitachi) (SEM) was used for study the surface morphology of the TiO$_2$/AgBiS$_2$ and Energy Dispersive Spectroscopy (EDS) was used to analysis the elemental compositions and distribution. The High-Resolution Field Emission Transmission Electron Microscope (JEM-

2100F, NEC Corporation) (TEM) was used for analysis the structural properties of the AgBiS$_2$ solar cells. To study the crystal formation of TiO$_2$ and AgBiS$_2$, X-ray Diffraction (XRD) was performed by a Polycrystalline X-Ray Powder Diffractometer (PANanalyticalX'pertHighscore diffractometer, X'Pert PRO MPD) with Cu Kα radiation. The surface composition of as-synthesized samples was analyzed using the X-ray photoelectron spectroscopy with a Thermos ESCALAB 250Xi multifunctional image electron spectrometer.

The current-voltage (I-V) characteristics of the solar cell were measured using the Zahner Zannium universal electrochemical workstation under one sun illumination, provided by a solar simulator at AM1.5G (Newport AAA solar simulator at 100 mW/cm^2). The absorption spectra of the AgBiS$_2$ films were recorded as a FTO reference using a Shimadzu 2450 UV–Vis spectrophotometer in the wavelength range of 300 to 1100 nm. External Quantum Efficiency (EQE) obtained as a function of wavelength from 300 nm to 1100 nm using the Bentham PVE300 photovoltaic characterization system. The open-circuit voltage decay (OCVD) was performed with RIGOL DS1054 digital oscilloscope. The stable voltage was achieved under illumination, after which the shutter was closed, and the voltage decay was recorded over a specific time interval. Electrochemical impedance measurements were performed with the Zahner Zannium universal electrochemical workstation equipped with a frequency response analyzer (Thalas) at a 10-mV amplitude AC signal and in the frequency range from 0.1 Hz to 1 MHz under the dark condition. Cyclic voltammetry (CV) experiments were carried out in a one-compartment three-electrode cell using the Zahner Zannium universal electrochemical workstation equipped with a frequency response analyzer (Thalas) at a 10-mV amplitude. The current was measured by applying a voltage between −1.2 and 1.2 V signal and at a frequency of 1 kHz in the dark. platinum was the counter electrode and Ag/AgCl saturated KCl as the reference electrode.

3. Results and discussions

3.1. Characterization of materials and electrodes

The primary goal of this study was to look into how the ZnS passivation layer affect the solar cell performance of Q-dot AgBiS$_2$ based light harvesting material. In this work, controlled deposition of ZnS passivation layers was performed in different interfaces such as TiO$_2$/(**ZnS(1)**)/AgBiS$_2$(hereafter A), TiO$_2$/AgBiS$_2$/(**ZnS(2)**)/electrolyte (hereafter B), and TiO$_2$/(**ZnS(1)**)/AgBiS$_2$/(**ZnS(2)**)/electrolyte (hereafter C), and the solar cell performance was investigated with respect to the ZnS layer and their surface passivation properties. The FTO/TiO$_2$/AgBiS$_2$ electrode without a ZnS layer was taken as the reference. The

formation and surface morphologies of various nanostructures were studied using XRD, SEM, and TEM analysis. X-ray diffraction (XRD) analysis of the reference and the electrode B was performed to confirm the crystalline structure and are shown in Fig. 1a and b respectively. To validate the phase composition of AgBiS$_2$, we have included the standard XRD pattern of AgBiS$_2$ in Fig. 1. As shown in Fig. 1a and b, the diffraction peaks corresponding to TiO$_2$, AgBiS$_2$ and ZnS are clearly visible in addition to the characteristic peaks of FTO substrate. The TiO$_2$ (P25) particles are characterized by strong diffraction peaks located at 2θ ≈ 25.27°, 27.49°, 36.08°,41.22°, 47.98°, 53.8°, 55.0°, 62.6°, and 68.64°, corresponding to the (101), (110), (101), (111), (200), (105), (211), (204), and (116) planes of anatase and rutile TiO$_2$ [32] The narrow and intense peaks indicate the formation of well-crystalline TiO$_2$ nanoparticles which would facilitate the electron transfer across the cell arrangement. Figure S1 shows the XPS investigation of AgBiS$_2$ nanocrystalline, confirming the presence of Ag, Bi, and S, as well as their predicted oxidation states (Ag$^+$, Bi^{+3}, S^{-2}), which are consistent with the AgBiS$_2$ phase.

The successful formation and the loading of AgBiS$_2$ Q-dots in TiO$_2$ matrix is confirmed by the observation of diffraction peaks at 2θ at 27.5°, 31.7°, 45.8°, 54.2°,and 56.4° corresponding to the (111), (200), (220), (311), and (222) crystalline planes of cubic phase AgBiS$_2$((PDF#21-1178) [30,31] However, it was noted that the diffraction peaks at 27.5° and 54.2° overlap with the diffraction peaks of TiO$_2$. On the other hand, diffraction peaks for ZnS for the case of FTO/TiO$_2$/AgBiS$_2$/ZnS should appear 2θ at 28.9°, 48.1° and 57.1° However, as shown in Fig. 1b, despite all three diffraction peaks for ZnS appear, diffraction peaks at 28.9° can be clearly seen while peaks at 48.1° and 57.1° overlap with the diffraction peaks of AgBiS$_2$ confirming the formation of ZnS layer (ICDD PDF 65-1691) [33] From the XRD patterns of FTO/TiO$_2$/AgBiS$_2$ and TiO$_2$/AgBiS$_2$/(**ZnS**), it can be deduced the formation of crystalline TiO$_2$, AgBiS$_2$, and ZnS (appeared to be less crystalline) in multilayer structures which is important for the better passivation of AgBiS$_2$ Q-dots and hence enhanced solar cell performance.

For the understanding of surface structure of FTO/TiO$_2$, FTO/TiO$_2$/AgBiS$_2$ and FTO/TiO$_2$/AgBiS$_2$/**ZnS**, SEM morphology images were taken and shown in Fig. 2a, b and c respectively. The corresponding EDX analysis are shown in Figures (2a-i and ii), (2b-i to 2b-vi) and (2c-i to 2c-vii). As shown in Fig. 2a, the pristine TiO$_2$ particles have smooth surface and spherical shape and are ~50 nm in size and the EDX results shown in Fig. 2a-i and ii confirm the presence of Ti and O. The SEM image of FTO/TiO$_2$/AgBiS$_2$ in Fig. 2b shows that the roughness of TiO$_2$ nanostructures increased after the deposition of AgBiS$_2$ Q-dots, as indicated by the magnified image in Fig. 2b, which shows uniformly covered Q-dots on
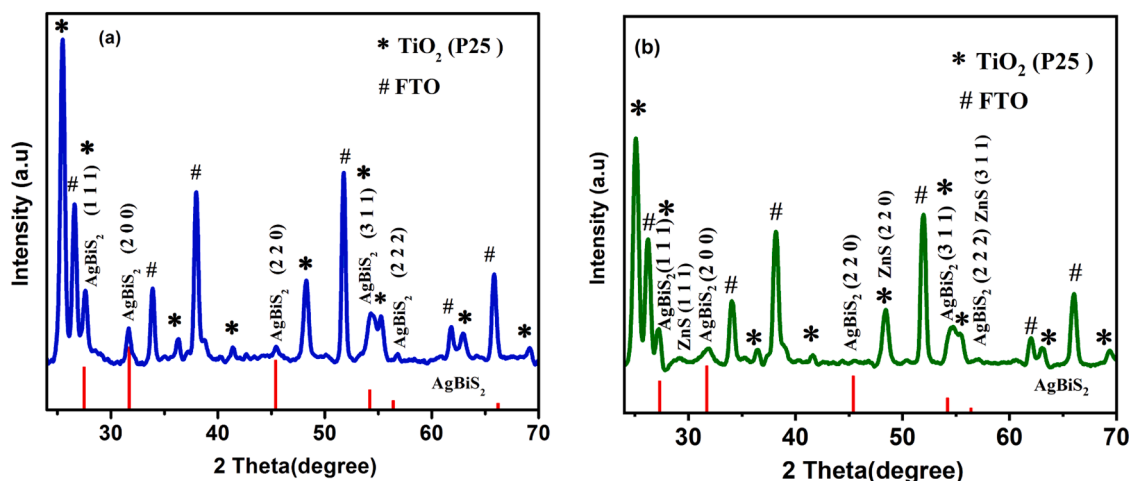

Fig. 1. XRD patterns of (a) FTO/m-TiO$_2$/AgBiS$_2$ and (b) FTO/m-TiO$_2$/AgBiS$_2$/**ZnS.**The standard diffraction patterns of AgBiS$_2$ are also given in (a) and (b).
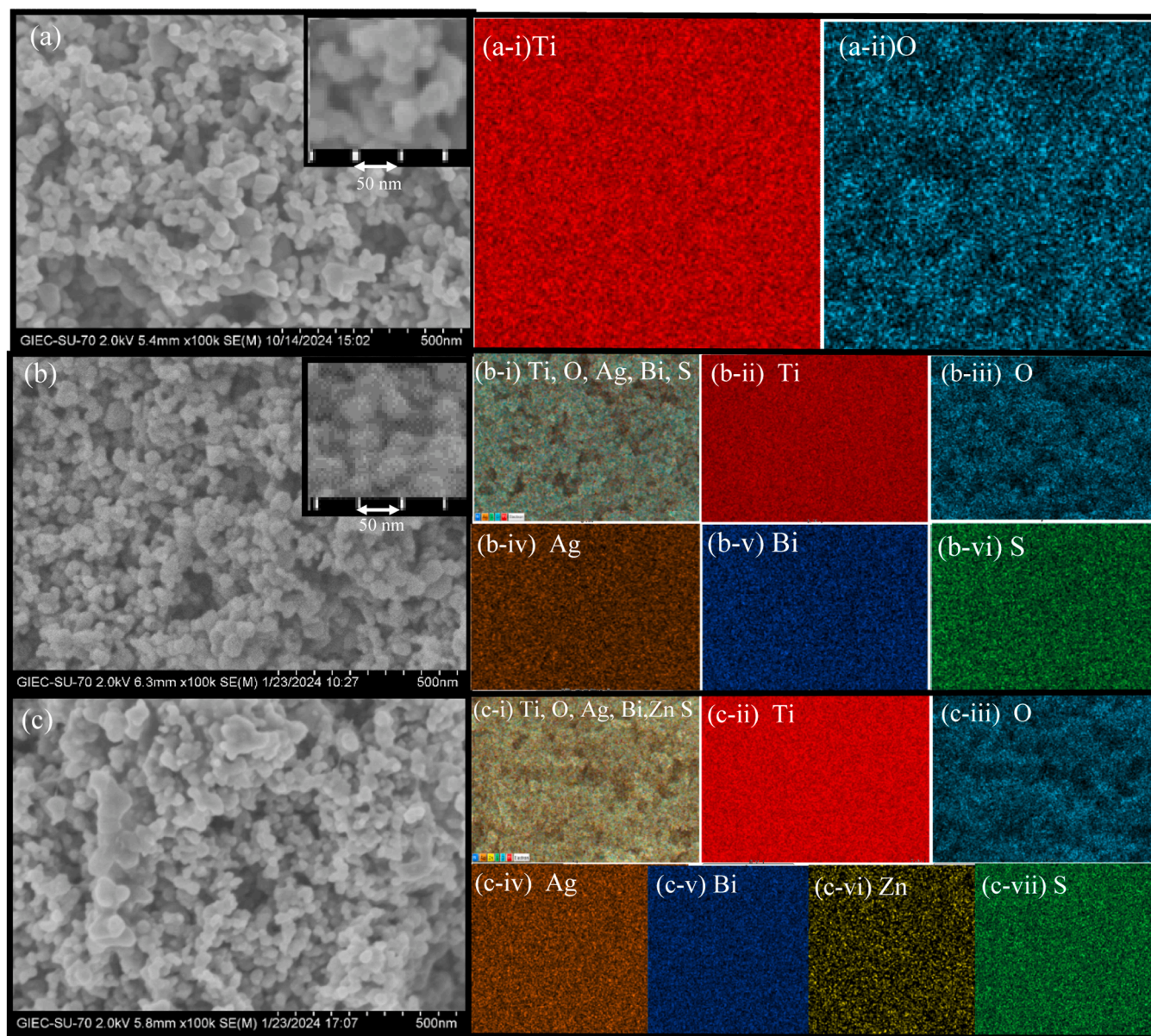
Fig. 2. SEM images of (a) FTO/m-TiO$_2$, (b) FTO/TiO$_2$/AgBiS$_2$ and (c) FTO/TiO$_2$/AgBiS$_2$/ZnS. The corresponding EDX results of these images are shown in Figure (2a-i and ii), (2b-i to 2b-vi) and (2c-i to 2c-vii) respectively.

the surface of TiO$_2$ nanoparticles. Although the deposition of AgBiS$_2$ quantum dots is clearly obvious, these quantum dots were not very visible in the SEM image. It is possible that the quantum dots had a size below the SEM resolution and were less visible in contrast to the larger TiO$_2$ particles. Furthermore, Fig. 2b-i to b-vi show distinct elemental distributions of Ag, Bi, and S, indicating the presence of AgBiS$_2$ on the surface of TiO$_2$ nanoparticles and hence the EDX results confirm the successful incorporation of Ag, Bi, and S into the TiO$_2$ matrix.

Coating of a thin ZnS layer on AgBiS$_2$ Q-dots loaded TiO$_2$ was noticeable in the SEM image of FTO/TiO$_2$/AgBiS$_2$/ZnS shown in Fig. 2c. The roughness and fine nanostructures observed in the SEM image of FTO/TiO$_2$/AgBiS$_2$ have disappeared as a result of ZnS deposition, and TiO$_2$/AgBiS$_2$ particles appear to be covered with a smear-like ZnS layer. The Zn and S distributions, along with the other elements in Fig. 2c-i to 2c-vii, confirm that the layer depicted in the SEM image is ZnS. The obvious visibility of the ZnS layer on the surface of Q-dot AgBiS$_2$ particles indicates the formation of uniform and continuous ZnS passivation layer. Furthermore, Figure S2 shows a cross-sectional SEM image and an EDX analysis of FTO/TiO$_2$/AgBiS$_2$/**ZnS**, which help in visualizing the

layered structure of the FTO/TiO$_2$/AgBiS$_2$/**ZnS**. The cross-sectional image shows an approximately 6 μm thick TiO$_2$ layer with equally dispersed Ag, Bi, S, and Zn components. Thus, the synthesis of AgBiS$_2$ and ZnS, as well as the successful passivation of AgBiS$_2$ Q-dots, can be confirmed using XRD diffraction patterns and SEM analysis.

The microstructure and crystallinity of TiO$_2$/AgBiS$_2$ before and after ZnS passivation were further investigated using TEM. Fig. 3a shows a clearly visible uniform distribution of nanometer-sized AgBiS$_2$ Q-dot particles on the surface of TiO$_2$ nanostructures. HRTEM images coupled with electron diffraction studies were used in analyzing the lattice fringe of the quantum dots, revealing their crystalline structure. The HRTEM image of TiO$_2$/AgBiS$_2$ shown in Fig. 3b revealed distinct lattice fringes with inter-planar spacing of 0.35 nm, which corresponds to the (101) plane of anatase TiO$_2$. The Q-dot particles seen on the HRTEM image in Fig. 3b are due to AgBiS$_2$ nanostructures, and their corresponding d-spacing 0.28 nm can be attributed to the (200) facet of AgBiS$_2$, while as shown in Figure S3, d-spacing 0.198 nm of Q-dot AgBiS$_2$ can be attributed to the crystalline plan (220) of AgBiS$_2$, confirming the presence of both (200) and (220) crystalline planes in AgBiS$_2$, which agree well with
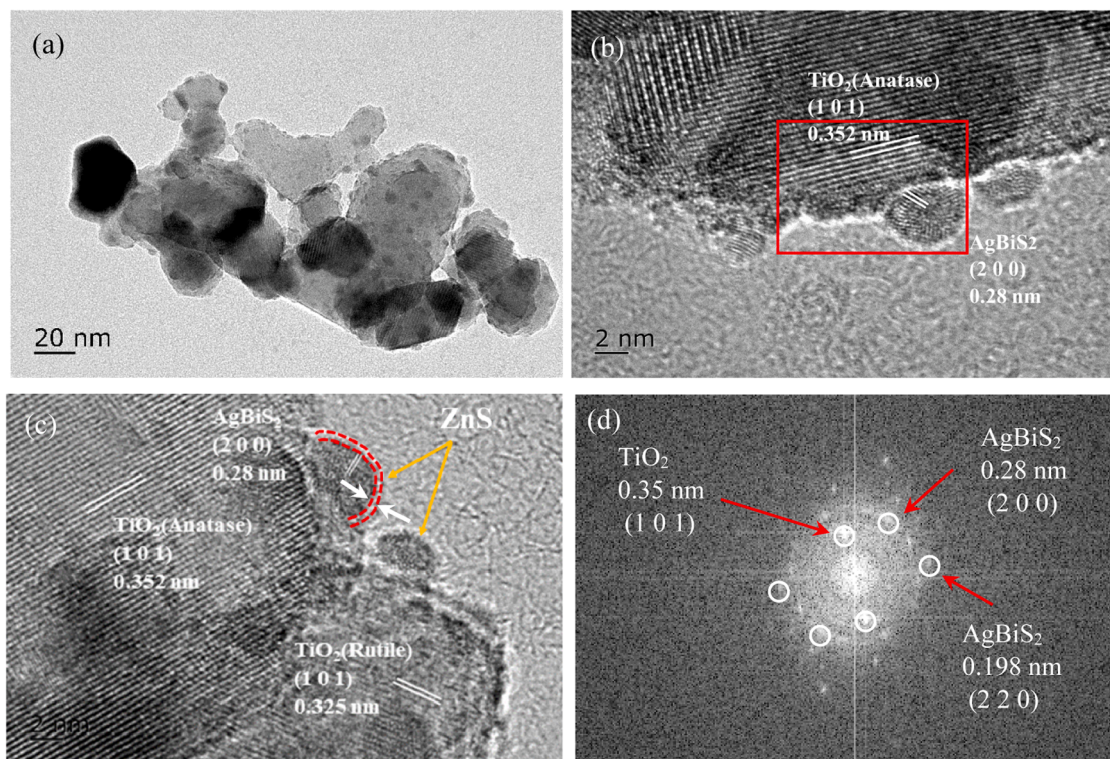
Fig. 3. TEM images of (a) $TiO_2/AgBiS_2$, (b) HRTEM image of $TiO_2/AgBiS_2$, (c) HRTEM image $TiO_2/AgBiS_2/ZnS$ and (d) Fast Fourier Transform (FFT) image of the red-colored region of the TEM image (b).
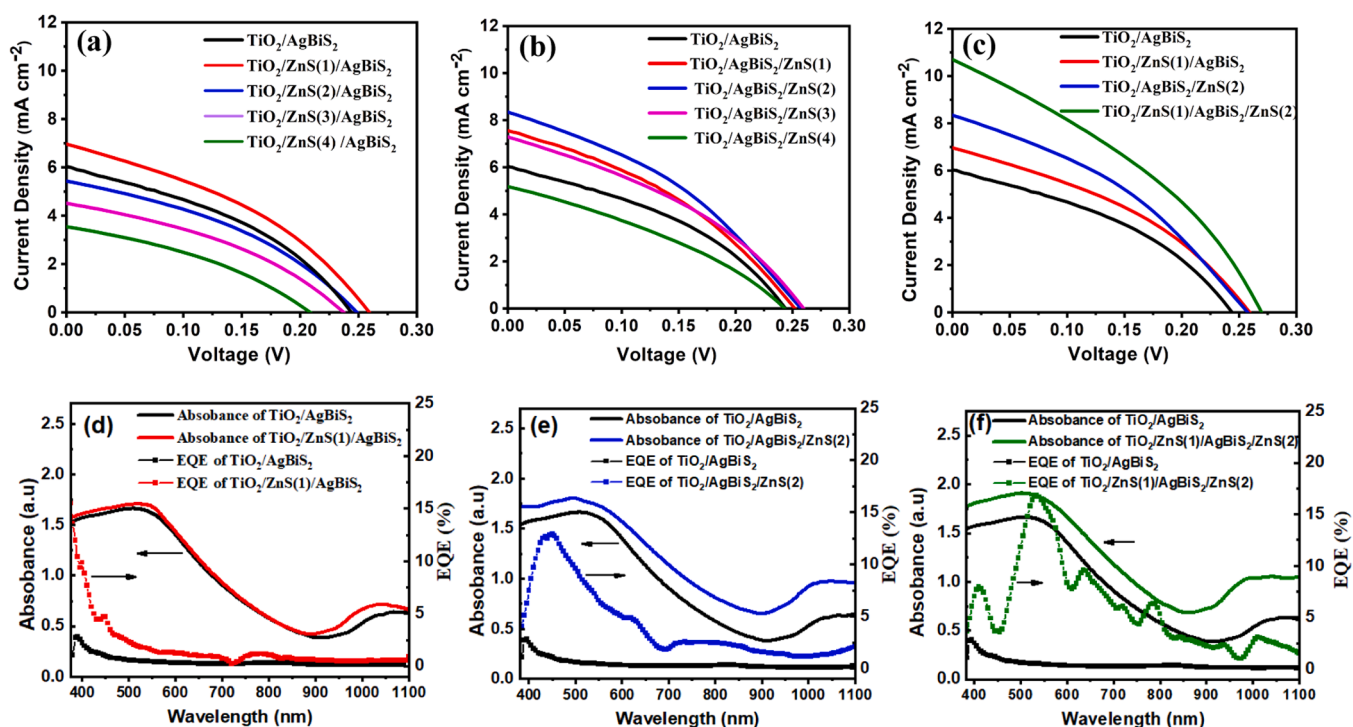

Fig. 4. Current density-voltage curves of (a) $FTO/TiO_2/ZnS(1)/AgBiS_2$, (b) $FTO/TiO_2/AgBiS_2/ZnS(2)$, (c) $FTO/TiO_2/ZnS(1)/AgBiS_2/ZnS(2)$; UV–Visible spectrocopy and EQE spectra of (d) $FTO/TiO_2/ZnS(1)/AgBiS_2$, (e) $FTO/TiO_2/AgBiS_2/ZnS(2)$ and (f) $FTO/TiO_2/ZnS(1)AgBiS_2/ZnS(2)$ with polysulfide electrolyte/ Cu_2S/Brass CE.

the XRD patterns shown in Fig. 1.

The TEM-EDS elemental mapping results shown in Figure S4 also strongly suggest that the $AgBiS_2$ quantum dots are uniformly distributed

in the TiO_2 layer, and that the $AgBiS_2$ Q-dot deposition method used in the hetero structure fabrication is capable of loading sufficient and homogeneous Q-dots on TiO_2 nanostructures. Additionally, to confirm the

crystalline planes, a Fast Fourier Transform (FFT) analysis was done on the red-colored portion of the TEM image shown in Fig. 3b. As shown in Fig. 3d, the bright point pair in the FFT correlates to a lattice pattern in the red-colored region, and by calculating the d-spacing of the lattice pattern associated to the bright point pair, the existence of TiO_2 and $AgBiS_2$ was established. The TEM images also clearly show that cubic $AgBiS_2$ quantum dots are embedded in the TiO_2 matrix. The HRTEM image of $TiO_2/AgBiS_2$ after deposition of a thin ZnS passivation layer is shown in Fig. 3c. As shown in Fig. 3c, in addition to fringe patterns (101) for TiO_2 (A) and (200) for $AgBiS_2$, there is also a fringe pattern (101) for TiO_2 (R), demonstrating the presence of both anatase and rutile TiO_2. On the other hand, Q-dot $AgBiS_2$ nanostructures are found to be covered with a thin amorphous layer, which could be owing to the ZnS passivation layer, which is not observed in the case of $TiO_2/AgBiS_2$ (Fig. 3b), confirming a conformal ZnS layer coating on Q-dot $AgBiS_2$ particles and thickness of ZnS layer was found to be ∼ 1–2 nm.

3.2. Solar cell performance

To elucidate the passivation effect of ZnS layer on solar cell performance of Q-dot $AgBiS_2$ electrodes, ZnS passivation layer was deposited as follows: A-($TiO_2/(\textbf{\textit{ZnS(1)}})/AgBiS_2$,) B-$TiO_2/AgBiS_2/(\textbf{\textit{ZnS(2)}})$ and both interfaces C-$TiO_2/(\textbf{\textit{ZnS(1)}})/AgBiS_2/(\textbf{\textit{ZnS(2)}})$ and solar cell performances of these electrodes were performed and the current versus voltage (J-V) curves of different electrodes under one sun illumination are shown in Fig. 4a, b and c respectively and the calculated solar cell performance from J-V curves are given in Table 1. The solar cell performance shown in Figure 4(a) and Table 1-I for the non-passivated and passivated TiO_2 by a thin ZnS layer indicated a marginal increase in the J_{sc} and V_{oc} resulting in an increase in overall efficiency from 0.56 % to 0.70 % after passivation. Furthermore, increasing the thickness of the ZnS layer resulted in a considerable reduction in solar cell performance due to the restricted flow of excited charge carriers from the $AgBiS_2$ light harvesting layer to the charge transport TiO_2 layer via the thicker insulating ZnS passivation layer. Though these findings suggest that electron transport TiO_2 layer passivation is less significant, the observed marginal increase in solar cell performance due to TiO_2 layer passivation by optimal ZnS passivation effectively balances TiO_2 surface passivation, and the ZnS layer acts as a barrier layer, effectively reducing recombination losses at the $TiO_2/AgBiS_2$ interface, thereby improving charge separation and photocurrent.

As shown in Fig. 4b, when the ZnS passivation was performed on the Q-dot $AgBiS_2$ particles of the electrode ($TiO_2/AgBiS_2/(\textbf{\textit{ZnS(2)}})$), a significant increase in the Jsc from 6.1 to 8.3 mA/cm^2 is noted, while a marginal increase in Voc is noted for non-passivated and passivated electrodes, indicating the significance of the passivation of the $AgBiS_2$-electrolyte interface (as given in Table 1-II). The effective passivation of Q-dot $AgBiS_2$ may help to reduce surface defects in $AgBiS_2$ Q-dots and improve charge collection efficiency by reducing electron hole recombination between the ZnS layer and the $AgBiS_2$ quantum dots, providing

a barrier to direct contact between the active layer and the electrolyte. Interestingly, the solar cell performance does not decline significantly with the increase of the ZnS passivation layer on $AgBiS_2/(\textbf{\textit{ZnS(2)}})$, as contrast to when a thicker ZnS layer is present on the TiO_2 layer [$TiO_2/(\text{ZnS}(1))/AgBiS_2$], which slows the transfer of excited charges from $AgBiS_2$ to TiO_2. However, the observed drop in solar cell performance caused by a thicker ZnS passivation layer could be attributed to light scattering effect and increase the charge transfer resistance as explained: The results show that the decline in solar cell efficiency with an increasing ZnS passivation layer is position-dependent. When a ZnS layer is placed between $TiO_2/ZnS/AgBiS_2$, improved light scattering by ZnS reduces the effective light absorption of $AgBiS_2$ quantum dots as well as photocurrent generation. When ZnS is deposited in the $AgBiS_2/ZnS/electrolyte interface, light scattering by ZnS allows increased light absorption by $AgBiS_2$ particles. However, the thicker ZnS film in the $AgBiS_2/ZnS/electrolyte interface increases series resistance, resulting in a decrease in charge transfer and device efficiency.

For the comparison of the passivation effect, I-V curves for non-passivated $TiO_2/AgBiS_2$ reference electrode, $TiO_2/(\textbf{\textit{ZnS(1)}})/AgBiS_2$ (electrode A), $TiO_2/AgBiS_2/(\textbf{\textit{ZnS(2)}})$ (electrode B), and double passivated $TiO_2/(\textbf{\textit{ZnS(1)}})/AgBiS_2/(\textbf{\textit{ZnS(2)}})$ (electrode C) are shown in Fig. 4c and the calculated solar cell parameters are given in Table 2. The observed efficiency increase order, Reference$<B<C<D$ suggested that the double passivated $TiO_2/(\textbf{\textit{ZnS(1)}})/AgBiS_2/(\textbf{\textit{ZnS(2)}})$ had the maximum efficiency, while the non-passivated reference $TiO_2/AgBiS_2$ had the lowest efficiency. Furthermore, it is clear that the passivation of Q-dot $AgBiS_2$ is more important than the passivation of the TiO_2 electron transport layer, and passivation of both TiO_2 and Q-dot $AgBiS_2$ demonstrated a synergic effect of defect passivation as well as charge recombination prevention. Indeed, the formation of ZnS layers at FTO/$TiO_2/\textbf{\textit{ZnS(1)}}/AgBiS_2/\textbf{\textit{ZnS(2)}}/polysulfide/CuS$ enhanced the blocking of recombination at both $TiO_2/AgBiS_2$ and $AgBiS_2/polysulfide$ interfaces and achieved the highest efficiency of 1.05 %. This increased passivation and better charge transport minimized charge carrier recombination losses, thereby optimizing photocurrent and overall PCE.

It is possible that the increased solar cell performance of Q-dot $AgBiS_2$ is related to changes in light absorption properties produced by variations and the placement of the ZnS passivation layer. However, as shown in Figure S5, the absorption properties of Q-dot $AgBiS_2$ does not significantly increase when optimum ZnS (two ZnS layers) is present as an outer-layer on the Q-dot $AgBiS_2$ particles. Thus, the observed improvement in solar cell efficiency with the ZnS passivation layer can be attributed to higher passivation and reduced charge carrier recombination losses. Furthermore, the comparison of EQE and absorption properties of electrodes A, B, and C in Fig. 4d, e, and f indicate despite their similar absorption properties, the double passivated electrode C has the highest EQE in the 400–1100 nm region and electrode B has the lowest EQE, indicating that defect passivation is the major factor determining the role of the ZnS layer.

The solar cell performance of ZnS passivated $AgBiS_2$ Q-dots highlighted the significance of the passivation effect of Q-dot-based $AgBiS_2$ light harvesting materials, which could be owing to the fact that passivation is known to reduce defect states, hence lowering trap-assisted charge recombination. Trap states in the TiO_2/Q-dots interface (i.e. $AgBiS_2$ Q-dots in this case) and inside the TiO_2 mesoporous

Table 1

Solar cell parameters for the passivation of (I) $TiO_2/(\textbf{\textit{ZnS}})/AgBiS_2$ and (II) $TiO_2/AgBiS_2/(\textbf{\textit{ZnS}})$ interfaces.

(I) Number of SILAR Cycle	J_{SC} (mA/cm^2)	V_{OC} (mV)	FF (%)	η (%)
0	6.1	245	37.5	0.56
1	6.9	258	39.3	0.70
2	5.6	243	38.2	0.52
3	4.5	237	37.5	0.40
4	3.5	209	36.9	0.27
(II)				
0	6.1	245	37.5	0.56
1	7.6	252	37.4	0.71
2	8.3	258	37.3	0.80
3	7.3	260	36.4	0.69
4	5.2	244	33.1	0.42

Table 2

Solar cell parameters of the $TiO_2/\textbf{\textit{ZnS(1)}}/AgBiS_2/\textbf{\textit{ZnS}}(2)/polysulfide$ electrolyte/Cu_2S.

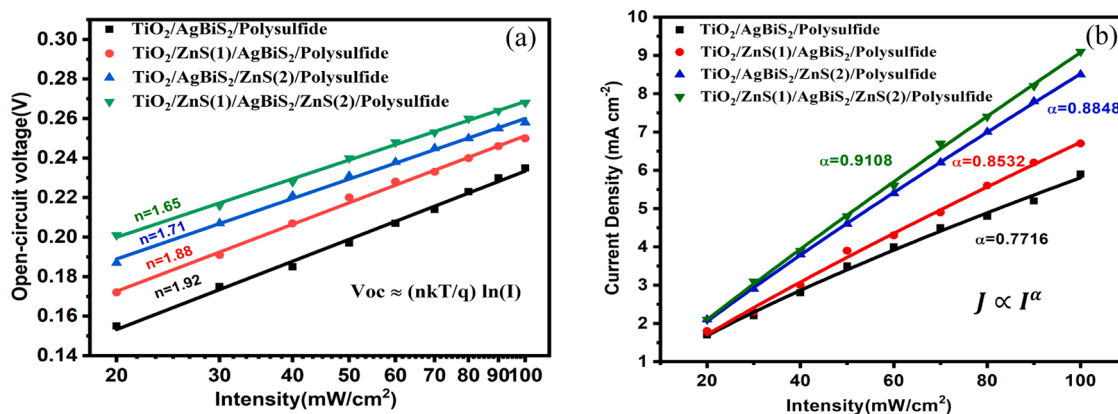| Cell configuration	J_{SC} (mA/cm^2)	V_{OC} (mV)	FF (%)	H (%)
$TiO_2/AgBiS_2/Electrolyte$	6.1	245	37.5	0.56
TiO_2/ZnS (1)$/AgBiS_2/Electrolyte$	6.9	258	39.3	0.70
$TiO_2/AgBiS_2/ZnS$ (2)$/Electrolyte$	8.3	568	37.3	0.80
TiO_2/ZnS (1)$/AgBiS_2/ZnS$ (2)$/$ Electrolyte	10.7	268	36.2	1.04

Fig. 5. (a) open-circuit voltage (V_{OC}) versus light intensity curves (b) current density (J) versus light intensity (I) curves.

network can lead to trap-assisted Shockley–Read–Hall (SRH) recombination, affecting charge carrier dynamics in solar cells [34,35] Hence, to better understand the significance of the ZnS passivation layer in controlling trap-assisted charge recombination, the diode ideality factor was determined using a logarithmic fit to the dependency of V_{OC} on light intensity. The ideality factor (n), calculated from open-circuit voltage (V_{OC}) against light intensity measurements, offers critical information about the major recombination mechanisms in quantum dot solar cells, as seen in Fig. 5(a) [36,37] The observed ideality factors for TiO2-AgBiS2, TiO2/(*ZnS(1)*)/AgBiS2, TiO2/AgBiS2/(*ZnS(2)*) and TiO2/(*ZnS(1)*)/AgBiS2/(*ZnS(2)*) are 1.92, 1.88, 1.71, and 1.65 respectively. The ideality factor which is a numerical indicator describes band-to-band or surface state recombination and a value greater than one can be related to trap-assisted SRH recombination. Hence, an ideality factor of 1.9 for TiO2-AgBiS2 without ZnS passivation, and the decrease in ideality factor with passivation clearly demonstrated a decrease in trap-assisted charge recombination after passivation. The ideality factor of TiO2/(*ZnS(1)*)/AgBiS2 (passivated TiO2) is greater than that of TiO2/AgBiS2/(*ZnS(2)*) (passivated AgBiS2) signify that the trap-assisted charge recombination is mainly due to Q-dot AgBiS2 materials. On the other hand, the lowest ideality factor for TiO2/(*ZnS(1)*)/AgBiS2/(*ZnS(2)*) revealed the relevance of passivation of both electron transport layer and light harvesting AgBiS2, which is consistent with the observed solar cell performance.

The current density (J) versus light intensity (I) curves shown for TiO2-AgBiS2, TiO2/(*ZnS(1)*)/AgBiS2, TiO2/AgBiS2/(*ZnS(2)*) and TiO2/(*ZnS(1)*)/AgBiS2/(*ZnS(2)*) electrode configurations in Fig. 5(b) provide valuable insights into the charge transport mechanisms and bimolecular recombination processes within the devices. The power-law relationship $J \propto I^\alpha$, where α is the exponent, describes is the exponent, explains how photocurrent (J) responds to variations in light intensity (I). When α is near to 1, it means the device has low recombination losses and the current is dominated by photogenerated charges. Trap-assisted recombination occurs when α values are significantly lower than one [36,37] The power-law exponents (α) TiO2-AgBiS2, TiO2/(*ZnS(1)*)/AgBiS2, TiO2/AgBiS2/(*ZnS(2)*) and TiO2/(*ZnS(1)*)/AgBiS2/(*ZnS(2)*) are 0.7716, 0.8532, 0.8848, and 0.9108, respectively. The variation of α values suggests more efficient passivation of surface defects in TiO2/(*ZnS(1)*)/AgBiS2/(*ZnS(2)*) by ZnS providing an efficient charge transport environment where bimolecular recombination during charge extraction is substantially decreased than the TiO2-AgBiS2 leading to reduced non-radiative recombination and enhanced charge separation and transport.

On the other hand, measuring the carrier life time (τ) in solar cells using open circuit voltage decay (OCVD) measurements over time reveals recombination behavior at the Q-dot electrolyte interface. The OCVD spectra of TiO2-AgBiS2, TiO2/(*ZnS(1)*)/AgBiS2, TiO2/AgBiS2/(*ZnS(2)*) and TiO2/(*ZnS(1)*)/AgBiS2/(*ZnS(2)*) electrodes are shown in Fig. 6a, and the τ is related to the open circuit voltage decay rates as given in Eq. (1), where K_B is the Boltzmann constant (1.38×10^{-23} J K^{-1}), T is the absolute temperature, q is the elementary charge and dV_{oc}/dt is the open circuit voltage decay gradient. Eq. (1) assumes that
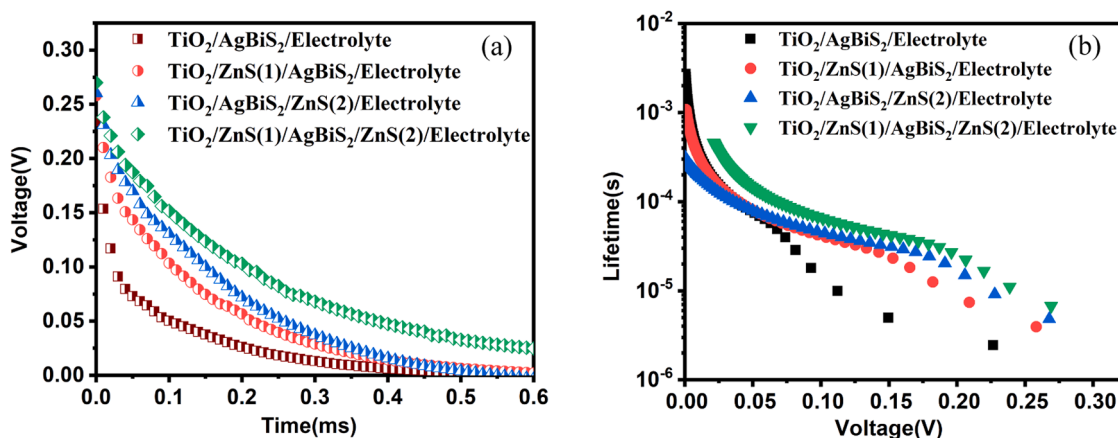

Fig. 6. (a) The open-circuit voltage decay (OCVD) curves and (b) The effective carrier lifetime calculated from the voltage decay curves versus open-circuit voltage for cell configurations: TiO2/AgBiS2, TiO2/(*ZnS(1)*)/AgBiS2, TiO2/AgBiS2/(*ZnS(2)*) and TiO2/(*ZnS(1)*)/AgBiS2/(*ZnS(2)*).
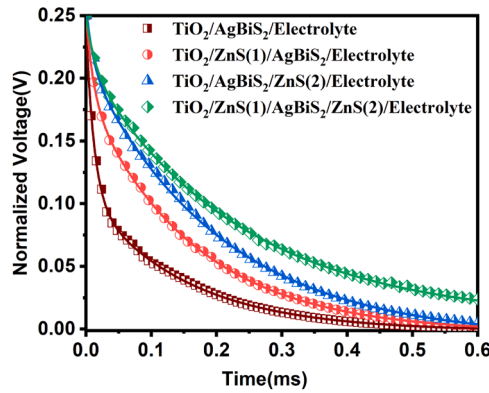
Fig. 7. Fitted open-circuit voltage decay (OCVD) curves for cell configurations: TiO$_2$/AgBiS$_2$, TiO$_2$/(**ZnS(1)**)/AgBiS$_2$, TiO$_2$/AgBiS$_2$/(**ZnS(2)**) and TiO$_2$/(**ZnS(1)**)/AgBiS$_2$/(**ZnS(2)**) with polysulfide electrolyte/Cu$_2$S.

Fig. 8. Electrochemical impedance spectroscopy (EIS) curves of TiO$_2$/AgBiS$_2$, TiO$_2$/(**ZnS(1)**)/AgBiS$_2$, TiO$_2$/AgBiS$_2$/(**ZnS(2)**) and TiO$_2$/(**ZnS(1)**)/AgBiS$_2$/(**ZnS(2)**) and the inset shown is the equivalent circuit used for fitting of EIS data.

electron recombination is linear with a first-order dependence on electron concentration, and that it only occurs with the electrolyte [38,39]

$$\tau = \left(\frac{K_B T}{q}\right)\left(\frac{dVoc}{dt}\right)^{-1} \tag{1}$$

The lifetime values obtained from Fig. 6a using Eq. (1) are shown in the Fig. 6b and the estimated lifetimes of TiO$_2$-AgBiS$_2$, TiO$_2$/(**ZnS(1)**)/AgBiS$_2$, TiO$_2$/AgBiS$_2$/(**ZnS(2)**) and TiO$_2$/(**ZnS(1)**)/AgBiS$_2$/(**ZnS(2)**) are 2.9, 8.8, 17.4 and 26.2 ms at 0.20 V, respectively. The OCVD results indicated that when a ZnS layer is coated on TiO$_2$ layer of the TiO$_2$/(**ZnS (1)**)/AgBiS$_2$ electrode, a notable slower voltage decay was observed compared to the TiO$_2$-AgBiS$_2$, and voltage decay was significantly slowed down after coating of ZnS on the AgBiS$_2$ layer of the TiO$_2$/AgBiS$_2$/(**ZnS(2)**) indicating that the major charge recombination process is via the Q-dot AgBiS$_2$ particle. The minimum voltage decay rate was noted for the electrodes in which both TiO$_2$ and AgBiS$_2$ were passivated with a ZnS layer.

However, as shown in Fig. 6, OCVD curves are nonlinear and decays exponentially and the nonlinear behavior of the OCVD curves can be effectively explained by the exponential fit of OCVD curves given in the Eq. (2) where V$_0$ is the open circuit voltage at the termination of excitation [40,41]

$$Voc(t) = \frac{kT}{q}\left[exp\left(\frac{qV_0}{K_B T} - 1\right)\right] exp\left(\frac{-t}{\tau}\right) \tag{2}$$

The exponential fitting findings for OCVD data in Fig. 7 according to Eq. (2) demonstrated that OCVD data cannot be fitted for a single exponential decay, implying that the electron recombination is a multi-step process. Furthermore, OCVD decay curves demonstrate a very fast decay process in the initial stage followed by a slow decay process and hence, the voltage decay curves were fitted with a two exponential decay process according to the Eq. (3) and fitted results are given in Fig. 7 and Table 3 [42,43]
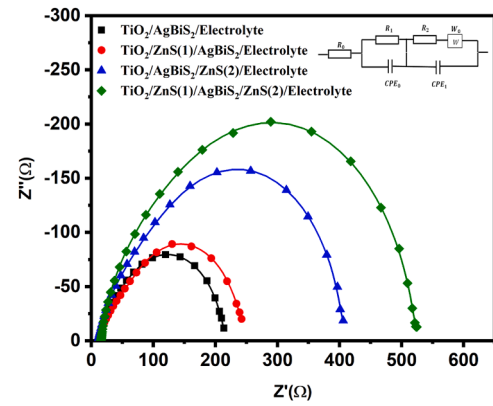
$$V = A_1 exp\left(-\frac{t}{\tau_1}\right) + A_2 exp\left(-\frac{t}{\tau_2}\right) + V_0 \tag{3}$$

The parameter A$_1$ determines the amplitude of fast recombination caused by intrinsic trapping-assisted recombination in AgBiS$_2$ and TiO$_2$, while τ_1 is the time constant for the same process. The sluggish recombination can be attributed to interfacial recombination at the AgBiS$_2$-electrolyte and AgBiS$_2$-TiO$_2$ interfaces and characterized by A$_2$ and τ_2. It is clear that the τ_1 value for fast recombination differs less significantly between non-passivated and passivated AgBiS$_2$ films, indicating it is an inherent property of the material. However, as explained later, the relative percentage of recombination loss caused by intrinsic trapping-assisted recombination can be mitigated by the passivation. On the other hand, passivation can reduce interfacial recombination at the AgBiS$_2$-electrolyte and AgBiS$_2$-TiO$_2$ interfaces, as evidenced by a significant increase in $\tau2$ values from 151.8 μs for the non-passivated (TiO$_2$-AgBiS$_2$ structure) to 234.1 μs for the double passivated TiO$_2$/(**ZnS(1)**)/AgBiS$_2$/(**ZnS(2)** design.

Interestingly, the variation in the contribution factor of parameters A$_1$ and A$_2$ with passivation reveals details about charge recombination in a multi-step process. The relative parameters A$_1$ and A$_2$ determine the amplitude of fast and slow recombination processes, respectively. Although τ_1 does not differ significantly between non-passivated and passivated structures, the observed relative A$_1$ and A$_2$ contribution factors of 55.7 and 44.7 % for the non-passivated structure indicate that charge loss is equally attributed to fast and slow charge recombination processes. While for the passivated TiO$_2$/(**ZnS(1)**)/AgBiS$_2$/(**ZnS(2)**) structure, the relative A$_1$ and A$_2$ factors are 13.7 % and 81.3 %, respectively, indicating that the trap-assisted charge recombination path has been significantly reduced, and the charge loss is primarily due to slow charge recombination processes. Overall, the results of the OCVD indicate that the ZnS layers successfully minimize the fast and slow charge recombination processes. Furthermore, despite the relative weight of A$_2$ was increased from 44 % to 84 %, time constant τ_2 was also increased significantly after ZnS passivation leading to the reduced interfacial recombination at AgBiS$_2$-electrolyte and AgBiS$_2$-TiO$_2$,

Table 3
Fitted results for open-circuit voltage decay (OCVD) curves.

Cell configuration	$A_1(A_1/(A_1 + A_2))$	$\tau_1(\mu s)$	$A_2(A_2/(A_1 + A_2))$	$\tau_2(\mu s)$
TiO$_2$/AgBiS$_2$/Electrolyte	0.5425 (55.7 %)	12.25	0.4311(44.3 %)	151.82
TiO$_2$/ZnS (1)/AgBiS$_2$/Electrolyte	0.2530(24.9 %)	11.61	0.7595(75.1 %)	164.79
TiO$_2$/AgBiS$_2$/ ZnS (2)/Electrolyte	0.1749(16.5 %)	10.64	0.8838(83.5 %)	204.02
TiO$_2$/ZnS(1)/AgBiS$_2$/ZnS(2)/Electrolyte	0.1511(15.6 %)	13.76	0.8166(84.4 %)	234.09

Table 4

Fitted results for Electrochemical impedance spectroscopy (EIS) curves.

Cell configuration	R_0	R_{ct}	R_{CR}
TiO$_2$/AgBiS$_2$/Electrolyte	12.6	36.4	163
TiO$_2$/ZnS (1)/AgBiS$_2$/Electrolyte	11.6	56.4	168
TiO$_2$/AgBiS$_2$/ ZnS (2)/Electrolyte	11.1	109	283
TiO$_2$/ZnS(1)/AgBiS$_2$/ZnS(2)/Electrolyte	15.4	111	394

thereby increasing charge collection efficiency and solar cell efficiency.

The impedance spectroscopic measurements and cyclic voltammetry (CV) analysis are also carried out to investigate the charge transport and recombination dynamics of passivated and non-passivated Q-dot AgBiS$_2$ electrodes. The Nyquist plots of TiO$_2$-AgBiS$_2$, TiO$_2$-AgBiS$_2$ [(TiO$_2$/(**ZnS (1)**)/AgBiS$_2$), TiO$_2$/AgBiS$_2$/(**ZnS(2)**) and TiO$_2$/(**ZnS(1)**)/AgBiS$_2$/(**ZnS (2)**)] are shown in Fig. 8 and the equivalent circuit employed to analyze the impedance data is given as an inset in Fig. 8. The equivalent circuit analysis yielded resistance values R_0 (series resistance), R$_{ct}$ (charge transport resistance), and R$_{cr}$ (charge recombination resistance) for passivated and non-passivated electrodes are given in Table 4. The series resistance R_0 describes the opposition to the flowing of the charge through the contact and layers. The calculated series resistance (R_0) values are small,this implies that charge transport is efficient through the material [44,45] However, R$_{ct}$ is found to be relatively higher for the ZnS layers coated samples. This may be due to that ZnS layer which acts as a physical and electronic barrier at the interface, and it may also impede the flow of electrons by creating an additional energy barrier for electron injection. This can result in increased R$_{ct}$ due to slower electron transfer. On the other hand, R$_{cr}$ refers to the resistance associated with the recombination of charge carriers (electrons and holes) within the device. The increase in the R$_{cr}$ from 163 to 394 Ω after passivation confirms that the growth of ZnS layers leads to a significant reduction in

recombination rates.

To analyze the recombination behavior in ZnS-coated AgBiS$_2$ Q-dot solar cells, cyclic voltammetry (CV) analysis was performed for passivated and non-passivated cell arrangements as shown in Figure S6. The results obtained from CV analysis indicated that the decrease in the peak current density after ZnS coating which can be attributed to the passivation of the Q-dot AgBiS$_2$ surface by minimizing the density of surface states which are known recombination sites. Hence as shown in schematically in Fig. 9, by carefully controlling the ZnS layer thickness and configuration, it is possible to effectively reduce charge recombination steps such as recombination at the AgBiS$_2$/electrolyte as well as TiO$_2$/electrolyte interfaces, recombination of charge carriers in TiO$_2$ with trapped holes in AgBiS$_2$ Q-dots that would eventually resulting in overall increase in solar cell performance.

4. Conclusion

The SILAR method was employed successful for the fabrication of Q-dot AgBiS$_2$ solar cell. However, the photovoltaic performance of Q-dot AgBiS$_2$ was found to be low, and the addition of a ZnS passivation layer improved solar cell performance, demonstrating the beneficial role of ZnS in increasing photocurrent. The intrinsic surface imperfections in AgBiS$_2$ that normally found to act as recombination centers can be passivated by coating a 1–2 nm thin ZnS layer, resulting in an improvement in both Voc and Jsc. The OCVD, CV, and EIS analyses revealed that the major recombination loss path is the charge recombination through the AgBiS$_2$-electrolyte interface, and that by carefully controlling the thickness and configuration of the ZnS layer, charge recombination can be effectively reduced, resulting in an overall increase in solar cell performance. Among all the fabricated electrodes, the dual ZnS layer structure composed of TiO$_2$/(**ZnS(1)**)/AgBiS$_2$/(**ZnS(2)**)/polysulfide/Cu$_2$S showed the greatest improvement in all evaluated
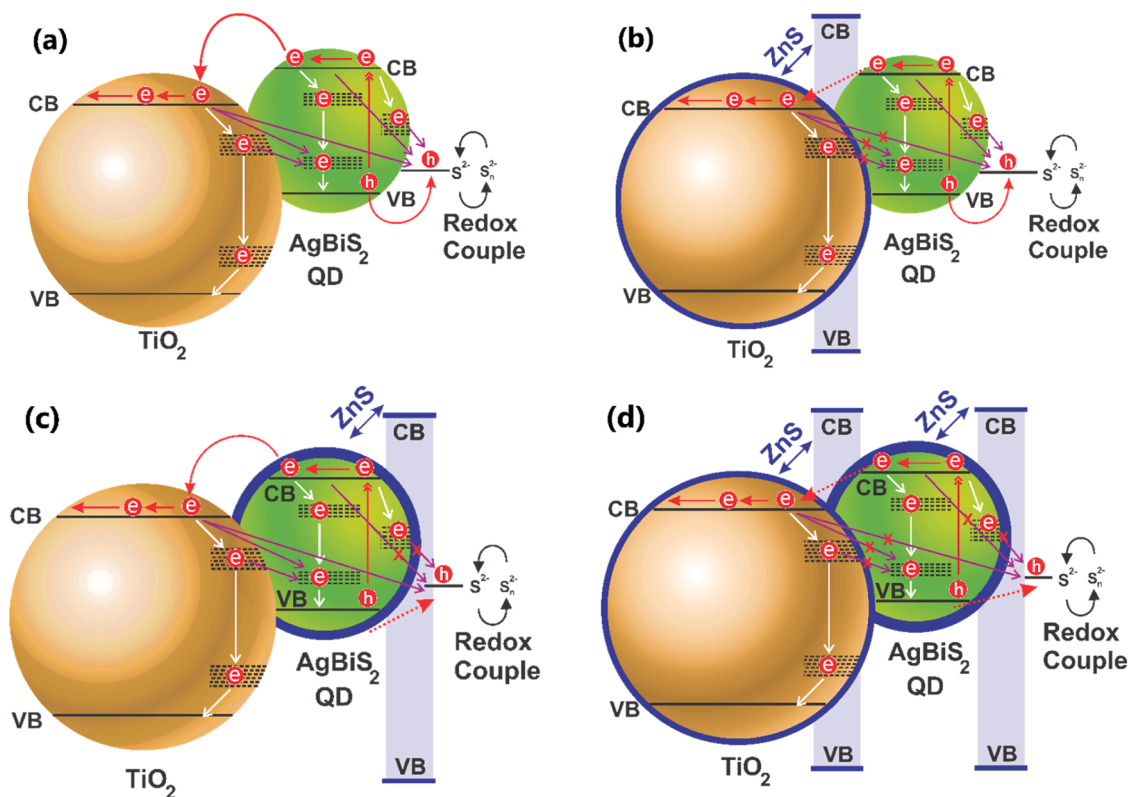

Fig. 9. Schematic illustrations of charge-transfer and carrier recombination processes of AgBiS$_2$ QD on TiO$_2$ for four cell configurations (a) TiO$_2$-AgBiS$_2$ (b) TiO$_2$/(**ZnS(1)**)/AgBiS$_2$, (c) TiO$_2$/AgBiS$_2$/**ZnS(2)** and (d) TiO$_2$/**ZnS(1)**/AgBiS$_2$/**ZnS(2)**) with polysulfide electrolyte.

photovoltaic parameters, indicating that layer thickness and composition had a significant impact on overall solar cell performance. Based on these findings, the ZnS layer may be improved further, as it has the potential to enhance the future generation of QDSCs and other renewable energy applications.

CRediT authorship contribution statement

Dimuthumal Rajakaruna: Writing – review & editing, Investigation, Data curation. **Hong-yi Tan:** Methodology, Data curation. **Chang-Feng Yan:** Writing – review & editing, Supervision. **Jayasundera Bandara:** Writing – original draft, Supervision, Formal analysis, Conceptualization.

Declaration of competing interest

The authors declare that they have no known competing financial interests or personal relationships that could have appeared to influence the work reported in this paper.

Supplementary materials

Supplementary material associated with this article can be found, in the online version, at doi:10.1016/j.electacta.2025.146173.

Data availability

Data will be made available on request.

References

[1] S. Akhil, R.G. Balakrishna, AgBiS 2 as a photoabsorber for eco-friendly solar cells: a review, J. Mater. Chem. A 10 (2022) 8615–8625.
[2] F. Tang, X. Yao, C. Ying, L. Xu, C.J.C.L. Shi, The preparation of AgBiS2 sensitized TiO2 nanorod array solar cells and photovoltaic performance of the corresponding solar cells, Chem. Lett. 51 (2022) 577–580, https://doi.org/10.1246/cl.220080.
[3] N. Akhtar, N. Nadeem, M. Yaseen, A. Jilani, A. Mahmood, U. Zubair, R. Haider, X. Yuan, M.J.M.C. Zahid, solar light-driven photocatalytic degradation potential of g-C3N4 based binary chalcogenides (AgBiS2/g-C3N4), Mater. Chem. Phys. 316 (2024) 129067, https://doi.org/10.1016/j.matchemphys.2024.129067.
[4] P.K. Gopi, C.G. Sanjayan, S. Akhil, C. Hunsur Ravikumar, S. Thitamadee, S. Kongpatanakul, R.G. Balakrishna, W. Surareungchai, Silver bismuth sulphide (AgBiS2)-MXene composite as high-performance electrochemical sensing platform for sensitive detection of pollutant 4-nitrophenol, Electrochim. Acta 498 (2024) 144616.
[5] X. Li, H. Yu, X. Ma, Z. Liu, J. Huang, Y. Shen, M. Wang, Thin film AgBiS2 solar cells with over 10 % power conversion efficiency enabled by vapor-assisted solution process treatment, Chem. Eng. J. 495 (2024) 153328.
[6] A. Senina, A. Prudnikau, A. Wrzesińska-Lashkova, Y. Vaynzof, F. Paulus, Cation exchange synthesis of AgBiS 2 quantum dots for highly efficient solar cells, Nanoscale 16 (2024) 9325–9334.
[7] P.-C. Huang, W.-C. Yang, M.-W. Lee, AgBiS2 semiconductor-sensitized solar cells, J. Phys. Chem. C 117 (2013) 18308–18314.
[8] P.-C. Huang, W.-C. Yang, M.-W. Lee, AgBiS2 semiconductor-sensitized solar cells, J. Phys. Chem. C 117 (2013) 18308–18314.
[9] N. Liang, W. Chen, F. Dai, X. Wu, W. Zhang, Z. Li, J. Shen, S. Huang, Q. He, J.J. C. Zai, Homogenously hexagonal prismatic AgBiS 2 nanocrystals: controlled synthesis and application in quantum dot-sensitized solar cells, CrystEngComm 17 (2015) 1902–1905, https://doi.org/10.1039/C4CE02405B.
[10] L. Mehdaoui, R. Miloua, M. Khadraoui, M.O. Bensaid, D. Abdelkader, F. Chiker, A. Bouzidi, Theoretical analysis of electronic, optical, photovoltaic and thermoelectric properties of AgBiS2, Phys. B Condens. Matter 564 (2019) 114–124.
[11] V.A. Öberg, M.B. Johansson, X. Zhang, E.M.J. Johansson, Cubic AgBiS2 colloidal nanocrystals for solar cells, ACS Appl. Nano Mater. 3 (2020) 4014–4024.
[12] S. Diedenhofen, M. Bernechea, K. Felter, F.C. Grozema, L. Siebbeles, Charge photogeneration and transport in AgBiS 2 nanocrystal films for photovoltaics, Sol. RRL 3 (2019) 1900075.
[13] X. Li, H. Yu, X. Ma, Z. Liu, J. Huang, Y. Shen, M. Wang, Thin film AgBiS2 solar cells with over 10 % power conversion efficiency enabled by vapor-assisted solution process treatment, Chem. Eng. J. 495 (2024) 153328.
[14] Y. Wang, S.R. Kavanagh, I. Burgués-Ceballos, A. Walsh, D.O. Scanlon, G. Konstantatos, Cation disorder engineering yields AgBiS2 nanocrystals with enhanced optical absorption for efficient ultrathin solar cells, Nat. Photonics 16 (2022) 235–241.
[15] Q. Zhong, B. Zhao, Y. Ji, Q. Li, X. Yang, M. Chu, Y. Hu, L. Li, S. Li, H. Xu, Solvent-engineering-assisted Ligand exchange strategy for high-efficiency AgBiS2 quantum dot solar cells, Angew. Chem. Int. Ed. 63 (2024) e202412590.
[16] J.T. Oh, H. Cho, S.Y. Bae, S.J. Lim, J. Kang, I.H. Jung, M. Choi, Y. Kim, Improved size distribution of AgBiS2 colloidal nanocrystals by optimized synthetic route enhances photovoltaic performance, Int. J. Energy Res. 44 (2020) 11006–11014.
[17] Y. Xiao, H. Wang, F. Awai, N. Shibayama, T. Kubo, J. Nakazaki, H. Segawa, Halide-ligand-dependent performance of AgBiS2 nanocrystal/ZnO heterojunction solar cells, Chem. Lett 51 (2022) 1004–1007.
[18] Y. Xiao, H. Wang, F. Awai, N. Shibayama, T. Kubo, H. Segawa, Eco-friendly AgBiS2 nanocrystal/ZnO nanowire heterojunction solar cells with enhanced carrier collection efficiency, ACS Appl. Mater. Interfaces 13 (2021) 3969–3978.
[19] Y. Xiao, H. Wang, F. Awai, N. Shibayama, T. Kubo, H. Segawa, Emission spectroscopy investigation of the enhancement of carrier collection efficiency in AgBiS2-nanocrystal/ZnO-nanowire heterojunction solar cells, ACS Appl. Mater. Interfaces 14 (2022) 6994–7003.
[20] I. Burgués-Ceballos, Y. Wang, G. Konstantatos, Mixed AgBiS 2 nanocrystals for photovoltaics and photodetectors, Nanoscale 14 (2022) 4987–4993.
[21] B. Zou, D. Chen, M. Qammar, P. Ding, P.K. Ko, W. Wu, S.B. Shivarudraiah, H. Yan, J.E. Halpert, In situ surface metal passivation on AgBiS2 nanocrystals for trap-reduced inverted solar cells, ACS Appl. Energy Mater. 7 (2024) 8271–8278.
[22] T. Manimozhi, J. Archana, M. Navaneethan, K. Ramamurthi, Shape-controlled synthesis of AgBiS2 nano-/microstructures using PEG-assisted facile solvothermal method and their functional properties, Appl. Surf. Sci. 487 (2019) 664–673.
[23] D. Liu, D. Cai, Y. Yang, H. Zhong, Y. Zhao, Y. Song, S. Yang, H. Wu, Solvothermal synthesis of carbon nanotube-AgBiS2 hybrids and their optical limiting properties, Appl. Surf. Sci. 366 (2016) 30–37.
[24] A. Manjceevan, J. Bandara, Robust surface passivation of trap sites in PbS q-dots by controlling the thickness of CdS layers in PbS/CdS quantum dot solar cells, Sol. Energy Mater. Sol. Cells 147 (2016) 157–163.
[25] A. Manjceevan, J. Bandara, Systematic stacking of PbS/CdS/CdSe multi-layered quantum dots for the enhancement of solar cell efficiency by harvesting wide solar spectrum, Electrochim. Acta 271 (2018) 567–575.
[26] J. Zhang, C. Sun, S. Bai, R. Luo, A. Chen, L. Sun, Y. Lin, Interfacial passivation of CdS layer to CdSe quantum dots-sensitized electrodeposited ZnO nanowire thin films, Electrochim. Acta 106 (2013) 121–126.
[27] F.A.N. Mawaddah, S.Z. Bisri, Advancing silver bismuth sulfide quantum dots for practical solar cell applications, Nanomaterials 14 (2024) 1328.
[28] S.Y. Bae, J. Yang, J.T. Oh, C.B. Lee, H. Song, B.R. Lee, H.M. Jin, K. Kim, J.P. Hong, Y. Kim, Understanding the cation-selective ligand passivation for AgBiS2 nanocrystal photovoltaics, Chem. Eng. J. 474 (2023) 145674.
[29] K. Tennakone, J. Bandara, P.K.M. Bandaranayake, G.R.A. Kumara, A. Konno, Enhanced efficiency of a dye-sensitized solar cell made from MgO-coated nanocrystalline SnO2, Jpn. J. Appl. Phys. 40 (2001) L732.
[30] J. Calva-Yáñez, O. Pérez-Valdovinos, E. Reynoso-Soto, G. Alvarado-Tenorio, O. Jaramillo-Quintero, M. Rincón, Interfacial evolution of AgBiS2 absorber layer obtained by SILAR method in hybrid solar cells, J. Phys. D Appl. Phys. 52 (2019) 125502.
[31] S. Akhil, J. Kusuma, R.G. Balakrishna, Green AgBiSe2/AgBiS2 core shell quantum dots for stable solar cells by robust SILAR method, J. Clean. Prod. 366 (2022) 132760.
[32] W. Li, R. Liang, A. Hu, Z.-H. Huang, Y. Zhou, Generation of oxygen vacancies in visible light activated one-dimensional iodine TiO2 photocatalysts, RSC Adv. 4 (2014) 36959–36966.
[33] N. Soltani, E. Saion, M. Hussein, M. Erfani, A. Abedini, G. Bahmanrokh, M. Navasery, P. Vaziri, Visible light-induced degradation of methylene blue in the presence of photocatalytic ZnS and CdS nanoparticles, Int. J. Mol. Sci. 13 (2012) 12242–12258.
[34] I. Mora-Sero, S. Giménez, F. Fabregat-Santiago, R. Gómez, Q. Shen, T. Toyoda, J. Bisquert, Recombination in quantum dot sensitized solar cells, Acc. Chem. Res. 42 (2009) 1848–1857.
[35] P. Calado, D. Burkitt, J. Yao, J. Troughton, T.M. Watson, M.J. Carnie, A.M. Telford, B.C. O'Regan, J. Nelson, P.R.F. Barnes, Identifying dominant recombination mechanisms in perovskite solar cells by measuring the transient ideality factor, Phys. Rev. Appl. 11 (2019) 044005.
[36] S. Shao, Z. Chen, H.-H. Fang, G. ten Brink, D. Bartesaghi, S. Adjokatse, L. Koster, B. J. Kooi, A. Facchetti, M. Loi, N-type polymers as electron extraction layer in hybrid perovskite solar cells with improved ambient stability, J. Mater. Chem. A 4 (2016) 2419–2426.
[37] S. Zhenhua, G. Sitbon, T. Pons, A. Bakulin, Z. Chen, Reduced carrier recombination in PbS - CuInS2 quantum dot solar cells, Sci. Rep. 5 (2015) 10626.
[38] Y. Zhang, G. Wu, I. Mora-Seró, C. Ding, F. Liu, Q. Huang, Y. Ogomi, S. Hayase, T. Toyoda, R. Wang, J. Otsuki, Q. Shen, Improvement of photovoltaic performance of colloidal quantum dot solar cells using organic small molecule as hole-selective layer, J. Phys. Chem. Lett. 8 (2017) 2163–2169.
[39] W. Li, Z. Pan, X. Zhong, CuInSe2 and CuInSe2-ZnS based high efficiency "green" quantum dot sensitized solar cells, J. Mater. Chem. A 3 (2014) 1649–1655.
[40] G. Gupta, A. Garg, A. Dixit, Electrical and impedance spectroscopy analysis of sol-gel derived spin coated Cu 2 ZnSnS 4 solar cell, J. Appl. Phys. 123 (2018) 013101.

[41] J.E. Mahan, T.W. Ekstedt, R.I. Frank, R. Kaplow, Measurement of minority carrier lifetime in solar cells from photo-induced open-circuit voltage decay, IEEE Trans. Electron. Devices 26 (1979) 733–739.

[42] J. Chang, Y. Kuga, I. Mora-Seró, T. Toyoda, Y. Ogomi, S. Hayase, J. Bisquert, Q. Shen, High reduction of interfacial charge recombination in colloidal quantum dot solar cells by metal oxide surface passivation, Nanoscale 7 (2015) 5446–5456.

[43] Y. Zhang, C. Ding, G. Wu, N. Nakazawa, J. Chang, Y. Ogomi, T. Toyoda, S. Hayase, K. Katayama, Q. Shen, Air stable PbSe colloidal quantum dot heterojunction solar cells: ligand-dependent exciton dissociation, recombination, photovoltaic property, and stability, J. Phys. Chem. C 120 (2016) 28509–28518.

[44] K. Sharma, V. Sharma, S.S. Sharma, Dye-sensitized solar cells: fundamentals and current status, Nanoscale Res. Lett. 13 (2018) 381.

[45] Y.-S. Lee, C. Gopi, A. Reddy, C. Nagaraju, H. Kim, High-performance of TiO2/CdS quantum dot sensitized solar cells with a Cu-ZnS passivation layer, New J. Chem 41 (2017) 1914–1917.